

Thermal Transport in Citrate-Capped Gold Interfaces using a Polarizable Force Field

Sydney A. Shavalier and J. Daniel Gezelter*

251 Nieuwland Science Hall, Department of Chemistry and Biochemistry,

University of Notre Dame, Notre Dame, Indiana 46556

E-mail: gezelter@nd.edu

Abstract

The interfacial thermal conductance from solvated gold nanostructures capped with sodium citrate was determined using reverse nonequilibrium molecular dynamics (RNEMD) methods. The surfaces of spherical nanoparticles and the (111) surfaces of fcc gold slabs were modeled using the density readjusting embedded atom method (DR-EAM) as well as with the standard embedded atom method (EAM), and the effects of polarizability on the binding preferences of citrate were determined. We find that the binding configurations of citrate depend significantly on gold surface curvature and are not strongly influenced by surface polarizability. The interfacial thermal conductance was also determined for the spherical nanoparticles and (111) surfaces, and we find that applying DR-EAM increases the interfacial thermal conductance for systems with spherical nanoparticles much more sharply than for systems with (111) surfaces. Through analysis of excess charge density near the interface, we find that inclusion of polarizability has a larger impact on image charge creation in nanospheres than it does for the planar (111) interfaces. This effectively increases the interaction strength to polar species in the solvent, yielding larger interfacial thermal conductance estimates for the nanospheres.

Introduction

Gold nanostructures have been studied extensively for use in photothermal therapies and other targeted biomedical applications.¹⁻⁸ While it is known that particle morphology can influence thermal conductivity,⁹⁻¹¹ there is no consensus yet on how heat transfer is affected by nanostructure curvature in more complex systems. Nanostructure viability for biomedical applications is also highly dependent on surface functionalization. Citrate is a protecting agent thought to work via creation of an electrical double-layer when adsorbed onto gold surfaces. Since it is also a common ion in physiological settings, it has shown promise as a biocompatible ligand.¹²⁻¹⁴

Molecular dynamics simulations of nanostructures are a useful method for recreating and explaining experimentally observed phenomena.¹⁵⁻¹⁷ The structures and binding of proteins¹⁸ and citrate overlayers¹⁹ on gold nanoparticles have both been studied via molecular simulation. In a re-

cent set of papers, Chong *et al.* studied the different binding motifs of citrate in various protonation states on the surfaces of gold particles.^{20,21} Perfilieva *et al.* stressed the importance of including gold polarizability when simulating with charged ligands such as citrate. They determined that the nature of citrate adsorption is influenced by whether the gold surface is polarizable.²²

The polarizable force fields previously used to study citrate capped nanoparticles^{19,22} included a rigid-rod dipole model in which a freely rotating dipole was attached to each gold atom. While the gold atoms were held fixed in space, the dipoles rotated when a charged species approached the gold surface.^{19,22} This is an elegant model, but the lack of atomic motion in the gold surfaces prevents simulation of vibrational contributions to thermal transport. Alternatively, the polarizable metal potential developed by Bhattarai *et al.* gives each metal atom an additional dynamic partial charge variable that represents fluctuations in local valence density. This partial charge is then propagated along with the nuclear degrees of freedom, allowing the charge distribution in the metal to respond to the local environment. This density readjusting embedded atom model (DR-EAM) is a superset of EAM-style potentials with the addition of Coulomb and self-potential terms.²³ In a study of the Au(111)-water interface, polarization of the gold surface using DR-EAM increased thermal conductance at the interface relative to EAM. This increase was likely due to an alteration in water ordering at the gold surface, as well as the image charge and image dipole interactions present in the DR-EAM potential.²⁴ The highly charged citrate anion is a natural application of DR-EAM, as the charges are likely to alter the surface behavior of gold when modeled using a polarizable potential.

Transport properties such as interfacial thermal conductance and thermal conductivity can be easily studied using reverse non-equilibrium molecular dynamics (RNEMD) methods. A minimally perturbative velocity shearing and scaling RNEMD method (VSS-RNEMD) has been developed which allows for periodic scaling of particle velocities,²⁵ and it has been extended for use in non-periodic simulations.²⁶ VSS-RNEMD was most recently used to study the solvent thermal conductivity and interfacial thermal conductance in a simulation of gold nanoarrays capped with phenylethanethiol in toluene and dichloromethane solvents. However, polarization of the gold sur-

face was not considered in this work as the systems did not contain charged species.²⁷ Interfacial thermal conductance has also been shown to increase with increasing surface curvature,^{28,29} but citrate's effect on this trend has not previously been studied. This study aims to determine the effect of gold surface polarization and curvature on heat transport in systems containing sodium citrate.

Computational Details

Gold nanostructures capped with citrate and solvated in water were simulated using RNEMD methods. Two kinds of simulations were carried out: One in periodic boundary conditions using slabs of fcc gold with the (111) surface exposed to the solvent, and one using spherical gold nanoparticles fully encased by a spherical shell of the solvent. Spherical nanoparticles were simulated using the non-periodic Langevin Hull algorithm in OpenMD to maintain an external pressure and temperature bath.²⁶ In both cases, RNEMD can effectively maintain a thermal flux either between two slabs (in periodic boundary conditions) or two concentric spheres (for the spherical nanoparticles). The system responds with a steady state thermal profile ($T(\mathbf{z})$ or $T(\mathbf{r})$) that exhibits a temperature jump at the interface between particle and solvent, enabling straightforward calculation of the interfacial thermal conductance.

The effects of gold surface polarization on thermal conductivity, interfacial thermal conductance, and citrate binding configurations were investigated. Force fields and system preparation procedures are briefly described below. Further details are available in the supplemental information (SI). A visual representation of the polarizable gold surface in a solvated spherical nanoparticle is shown in Figure 1. With DR-EAM, the charges on the gold atoms respond to the species in closest proximity.

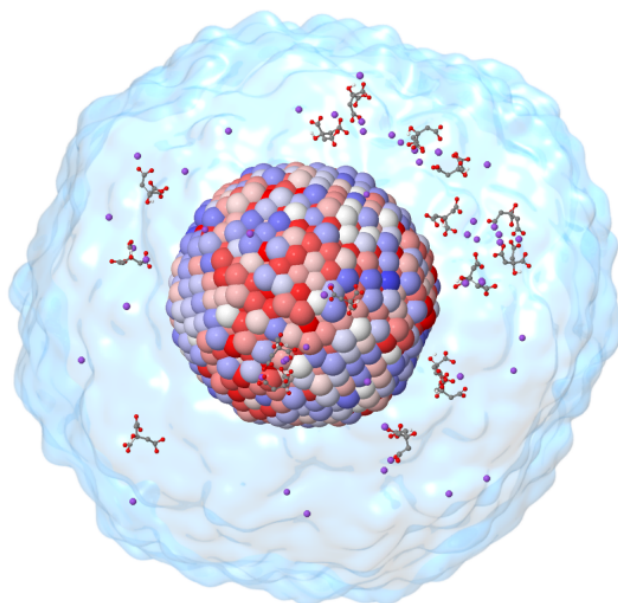


Figure 1: Solvated gold nanoparticle represented by a fluctuating density force field which assigns partial charges to metallic sites. The partial charge on each gold atom is shown using a Red-White-Blue gradient in which red atoms are more negatively charged ($-0.1e$) and blue are more positively charged ($+0.1e$). Surface metal atoms respond to solvent charges directly adjacent to the surface, and are therefore primarily dominated by instantaneous fluctuations in the solvent structure. Sodium citrate is shown in standard CPK colors: carbon atoms are grey, oxygen atoms are red, hydrogen atoms are white, and sodium atoms are purple. All water atoms are rendered as translucent. A portion of the solvent cloud has been removed for visibility.

Force Fields

In this work we utilized two separate models for citrate anions and sodium counter-ions. One set of sodium citrate interactions used charges and Lennard-Jones parameters from Chong *et al.*²⁰ The central backbone of the citrates were kept rigid by fixing the bond lengths between the hydroxyl oxygen – hydroxyl hydrogen (0.945 Å), central carbon – hydroxyl oxygen (1.41 Å), and central carbon – central carboxylate carbon (1.529 Å). These constraints prevent unphysical intramolecular hydrogen bonding between the hydrogen and central carboxylate oxygens, which has been previously observed in this and other related citrate models.^{21,30} To study the effect of these con-

straints, we also simulated planar interfaces using all-atom sodium citrate interaction parameters from Wright *et al.* which include all hydrogen atoms and do not require any internal constraints.³⁰

For all systems studied, rigid body SPC/E water molecules were used as solvent.³¹ For interactions between gold atoms and SPC/E water atoms, we utilize a Mie potential with a functional form taken from Dou *et al.*³² and subsequently modified to facilitate citrate binding. Further details are available in the SI.

For nonpolarizable systems, gold interactions were taken from the EAM parameterization in Zhou *et al.*³³ For polarizable systems, parameters were taken from Bhattarai *et al.*²⁴ From these components and parameters, four unique systems of interest were constructed: A non-polarizable fcc slab system, a polarizable fcc slab system, a system containing a 20 Å radius non-polarizable spherical nanoparticle, and a system containing another identical (but polarizable) nanoparticle. All interaction parameters can be found in Tables S1 – S11 in the SI.

Simulation Protocol

Planar gold (111) surfaces were constructed with a lattice constant of 4.08 Å using the OpenMD utility slabBuilder.³⁴ Following surface construction, Packmol³⁵ and another OpenMD utility were used to combine the nanostructures with molecular models for sodium citrate and SPC/E water. After an initial 20 ps structural relaxation (NVT), the systems were equilibrated in an isobaric-isothermal (NPT) ensemble for 400 ps to find a suitable box volume, and then thermally equilibrated to a temperature of 300 K in a canonical (NVT) ensemble for 200 ps. This was followed by a 200 ps equilibration in the microcanonical (NVE) ensemble. The spherical nanoparticles were built with a radius of 20 Å and a lattice constant of 4.08 Å using nanoparticleBuilder, another OpenMD utility.³⁴ Atoms were given velocities sampled from a Maxwell-Boltzmann distribution at 5 K, and the nanospheres underwent incremental structural relaxation at 5 K, 100 K, 200 K, and 300 K using normal thermostatting methods. Metallic structures were subsequently combined with the solvent (which was built using Packmol³⁵ and another OpenMD utility³⁴). The central gold atom at the center of each nanoparticle were given a large mass to anchor the particle to the

origin and prevent drifting. Prior to sampling, the systems were simulated with a Langevin Hull integrator for 1 ns.²⁶ After these equilibration steps, the distributions of citrate configurations were sampled every 20 ps over a 2 ns period (in the microcanonical ensemble for slab systems and using a Langevin Hull integrator for nanoparticle systems). Further details regarding the systems simulated in this work are shown in Table 1. All systems have similar citrate concentrations and water densities.

Table 1: Structures simulated in this work

	Nanospheres	(111) Slab
Metallic structure	$r = 20 \text{ \AA}$	$30 \times 29 \times 19 \text{ \AA}$
System size	$r \sim 40 \text{ \AA}$	$30 \times 29 \times 172 \text{ \AA}$
Gold volume (\AA^3)	33,510	16,530
Solvent volume (\AA^3)	234,572	133,110
N_{Gold}	1985	1080
N_{Water}	8095	4704
N_{Citrate}	17	10
N_{Sodium}	51	30
[Citrate] (M)	0.120	0.126
ρ_{water} (g/cm^3)	1.03	1.07

We have adopted the categorization of citrate binding motifs from Chong *et al.*²⁰ In the tall configuration, the citrate is bound to the gold surface solely through one terminal carboxylate. In the bridge configuration, the citrate is bound through both terminal carboxylates. The 0-arm, 1-arm, and 2-arm configurations describe a citrate bound via either the central hydroxyl or central carboxylate (or both) along with zero, one, or two terminal carboxylates, respectively. A citrate is considered bound to the surface if an oxygen is within 3.5 \AA of the gold surface. A visual representation of these configurations is shown in Figure 2.

The percentage of bound citrates and gold surface coverage were also determined and are shown in Table 2. To determine the percentage of bound citrates, we examined how many citrates

contained at least one oxygen that was within 3.5 Å of the gold surface at any point during the configuration sampling time. To determine the gold surface coverage, we calculated the average number of gold atoms which were within 3.5 Å of a citrate oxygen during the same sampling period.

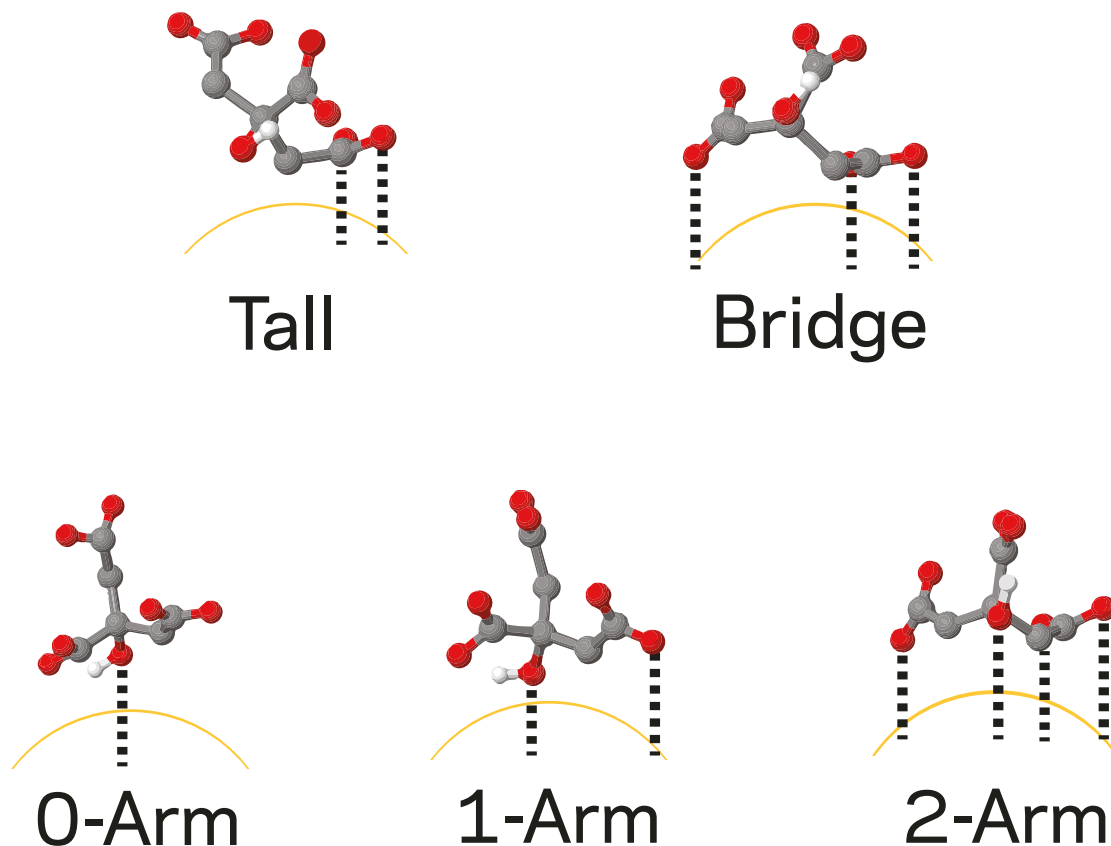


Figure 2: Representative snapshots of each of the citrate configurations introduced by Chong *et al.*²⁰ and studied in this work. The gold curves represent the surface of the gold structure in each configuration. Each oxygen that is bound to the gold surface is represented by a black dotted line.

Following surface characterization, RNEMD simulations were carried out for at least 1 ns with an applied thermal flux, $J_z = 2.5 \times 10^{-6} \text{ kcal mol}^{-1} \text{ \AA}^{-2} \text{ fs}^{-1}$ for periodic systems and $J_r = 1.8 \times 10^{-6} \text{ kcal mol}^{-1} \text{ \AA}^{-2} \text{ fs}^{-1}$ for non-periodic systems. A thermal flux was applied to all systems for at least 1 ns. The flux values were chosen so the heat rate through the metal/solvent interface was nearly identical in the planar and spherical geometries. Relatively small flux values also ensure that the systems remain in a state close to ambient conditions, limiting thermally-induced

density changes in the solvent phase which could interfere with measurements of the interfacial conductance. We studied the thermal profile after flux application times of up to 1 ns, and the results can be seen in Figure S3 in the SI. Under steady state conditions, temperature discontinuities formed at the boundaries between the gold and the solvent, and a thermal gradient developed in the solvent.

The open source molecular dynamics engine OpenMD was used for all simulations.³⁴ The RNEMD methods of Kuang *et al.* were adopted for periodic systems²⁵ and those of Stocker *et al.* were adopted for non-periodic systems.²⁶

Calculating Thermal Transport Properties

Fourier’s law allows us to compute the thermal conductivity, λ , in a bulk material by connecting an applied thermal flux, \mathbf{J} , to a measured temperature gradient,

$$\mathbf{J} = -\lambda \nabla T. \quad (1)$$

In the planar (slab) systems, this can be done using the z -projection of the thermal flux, J_z , which is an imposed perturbation in our RNEMD simulations. The resulting thermal gradient also develops along the z -axis. The interfacial thermal conductance, G , is given by

$$G = \left(\frac{J_z}{\Delta T} \right) \quad (2)$$

where ΔT is the temperature difference across the interface of interest. Outside of the interface, bulk materials develop linear thermal gradients due to bulk thermal conductivity. ΔT is the sudden change in temperature at the boundary between the solid and liquid, seen in Figure 5. Jiang *et al.* recently introduced the Atomistic Nodal Approach (ANA) for calculating localized thermal fluxes in complex systems when a temperature gradient is imposed.¹¹ This corresponds to a forward

version of NEMD. We note that *reverse* NEMD, because it imposes \mathbf{J} directly, does not require this treatment.

Another advance in Jiang *et al.* was the use of continuity equations to estimate λ and G values from significant portions of the thermal profiles.¹¹ For periodic (slab) systems, the solid portion of the thermal profile can be modeled by integrating Fourier's law starting at the center of the box,

$$T_s(z) = T_s(c) - |z - c| \left(\frac{J_z}{\lambda_s} \right) \quad (3)$$

where c is the center of the solid region. Here J_z is the thermal flux projected along the z -axis, in a direction normal to the interface, and $T_s(c)$ and λ_s are fit to the thermal profile. Similarly, the liquid portion of the thermal profile is modeled with a nearly identical function, but with a liquid state thermal conductivity,

$$T_l(z) = T_l(c) - |z - c| \left(\frac{J_z}{\lambda_l} \right) \quad (4)$$

To find the temperature jump at the interface, $\Delta T = T_s(z) - T_l(z)$, Eqs. (3) and (4) are stitched together using two hyperbolic tangent functions with one located at $z = l$ and the other at $z = r$, the left and right boundaries between the gold and solvent, respectively. The continuity equation describing the temperature profile is, therefore,

$$T(z) = \frac{1}{2} \left(\tanh \left(\frac{z-l}{d} \right) - \tanh \left(\frac{z-r}{d} \right) \right) T_s(z) + \left(1 - \frac{1}{2} \left(\tanh \left(\frac{z-l}{d} \right) - \tanh \left(\frac{z-r}{d} \right) \right) \right) T_l(z), \quad (5)$$

where d is a parameter which describes the width of the boundary between the solid and liquid regions. This continuity equation is similar to the one utilized by Jiang *et al.* with an alteration of the function used for switching between the two regions. To find the two temperature jumps, $\Delta T_r = T_s(r) - T_l(r)$ and $\Delta T_l = T_s(l) - T_l(l)$, we can then use the locations of l and r from the fit temperature profile to estimate the interfacial thermal conductance G .

For systems involving spherical nanoparticles, we can use another modified continuity equation

from Jiang *et al.*¹¹ The solid portion of the thermal profile is integrated assuming a constant heat flux through the particle surface located at R_c ,

$$T_s(r) = \left(\frac{J_r}{\lambda_s} \right) \left(\frac{R_c^2}{r} - R_c \right) + T_s(R_c) \quad (6)$$

where J_r is the applied flux and R_c is the radial cutoff between the solid and fluid. The liquid portion of the thermal profile is modeled similarly where

$$T_f(r) = \left(\frac{J_r}{\lambda_f} \right) \left(\frac{R_c^2}{r} - R_c \right) + T_f(R_c). \quad (7)$$

These are also stitched together with two hyperbolic tangent functions, yielding a continuity equation

$$T(r) = \frac{1}{2} \left(1 + \tanh \left(\frac{r - R_c}{w} \right) \right) T_s(r) + \frac{1}{2} \left(1 - \tanh \left(\frac{r - R_c}{w} \right) \right) T_f(r). \quad (8)$$

An alternative approach is to assume that the interface has a finite thickness, and to compute interfacial thermal conductance from a series approximation for the Kapitza resistance

$$\frac{1}{G} = R_K = \frac{1}{q_r} \sum_i 4\pi r_i^2 (T(r_{i+1}) - T(r_i)) \quad (9)$$

where q_r is the radial heat rate and $T(r_i)$ is the temperature of the spherical shell at radius r_i . This model assumes thermal resistance is additive for a series of concentric spherical shells, each with a well-defined average temperature, surface area, and a constant heat rate that traverses all of the shells. For the nanoparticles, this is essential as the interface is a broad region that extends outward from the metal surface by roughly 10 Å.

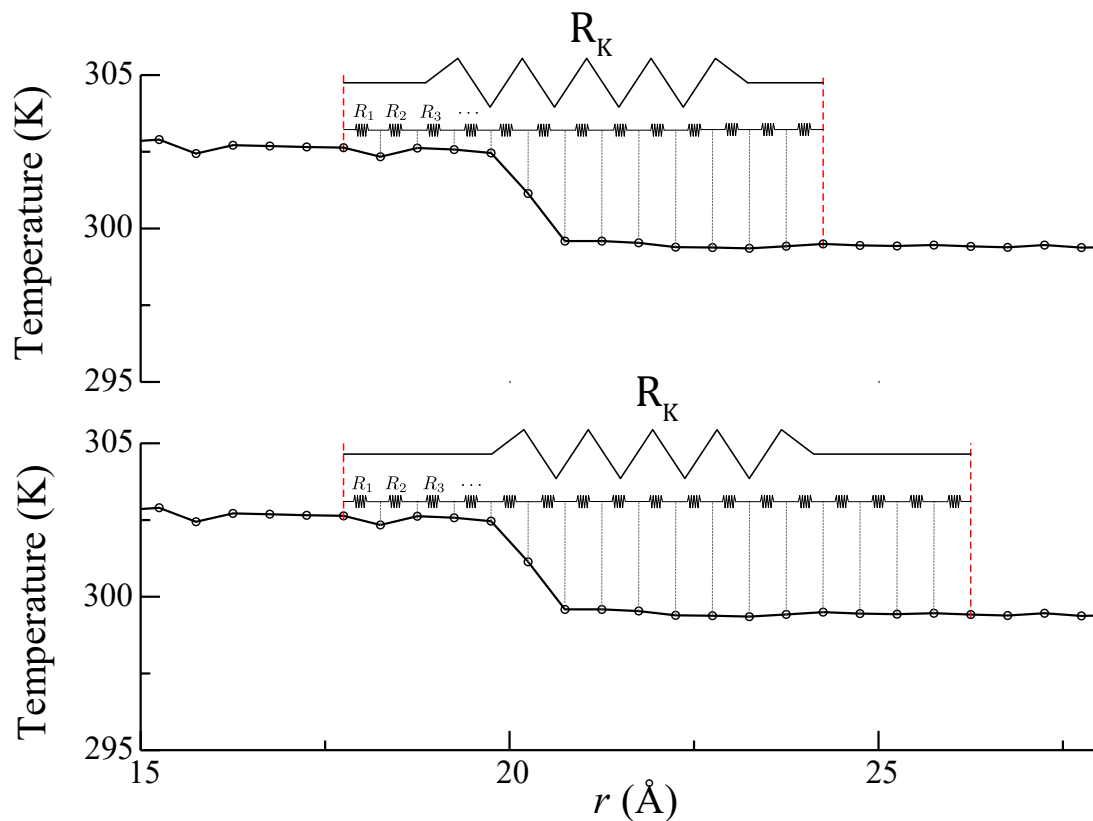


Figure 3: Estimating interfacial conductance between a nanoparticle and solvent using a series approximation for the Kapitza resistance (Eq. (9)). The number of spherical shells contributing to interfacial resistance can be varied easily. *Top*: a thin interfacial region comprising a radius of 17.75 (inside the gold particle) to 24.25 Å (just outside the first solvation shell). *Bottom*: a thicker interfacial region ending at 26.25 Å. The advantage of using Kapitza resistance is that the width of the interfacial region can be used as a convergence parameter, which is not possible when estimating temperature drops from solid and liquid temperatures projected onto a single interface, e.g. Eq. (8).¹¹

Results and Discussion

Citrate Surface Coverage and Binding

Surface coverage was measured for the citrate molecules as a fraction of bound vs. total citrate, as well as for the surface itself, using the fraction of surface gold atoms that are within 3.5 Å of a citrate ion. In either case, the criterion for binding is similar. Gold atoms within 3.5 Å of any citrate atom are considered bound to a citrate, and citrate ions with an oxygen atom within 3.5 Å of gold are considered bound to the surface. The fraction of bound citrates (see Table 2) appear to be highly curvature dependent, with planar (111) slabs exhibiting more bound citrate than the nanoparticles. Polarization of the gold surface appears to slightly decrease the fraction of bound citrate as well as the gold surface coverage. In order to bind to the gold surface, a citrate molecule must compete with water molecules near the surface. The SPC/E oxygen is more negatively charged than the citrate carboxylate oxygens and the citrate hydroxyl oxygen. When using a polarizable metal, the gold surface will respond to higher oxygen charges with a larger positive surface charge, yielding a stronger binding with SPC/E water. This likely explains the decrease in citrate binding when the gold surface is polarizable.

Table 2: Coverage of Citrates on the Gold Surface

		bound citrate (%)	Au surface coverage (%)
Au (111) slab	non-polarizable	31 ± 11	5.5 ± 1.6
	polarizable	26 ± 10	4.5 ± 1.4
Au nanoparticle	non-polarizable	20 ± 8	2.9 ± 0.8
	polarizable	13 ± 4	1.8 ± 0.6

Citrate binding preferences are shown in Figure 4. When the gold surface is polarized, there is very little difference in binding across nanostructure geometries. For the slab systems, the 0-arm configuration is most heavily favored. For the nanoparticle systems, the percentage of 0-arm and 1-arm configurations are nearly identical. Therefore, we can conclude that a significant number of bound citrates position themselves with the binding central groups perpendicular to the plane

of the gold surface and the terminal carboxylates. Since the citrate molecules are likely parallel to the plane of the gold surface, the increased curvature of the nanoparticle would result in a comparatively greater percentage of citrates bound in the 1-arm configuration. This behavior also reduces the 2-arm and bridge binding, in which both terminal carboxylate groups bend toward the surface. As modeled here, the citrate molecules are too rigid for this degree of bending to occur to a significant degree. Since the 0-arm, 1-arm, and 2-arm configurations can be bound by one or both of the central groups, the distributions of these sub-configurations were also determined and can be found in Figure S4 in the SI.

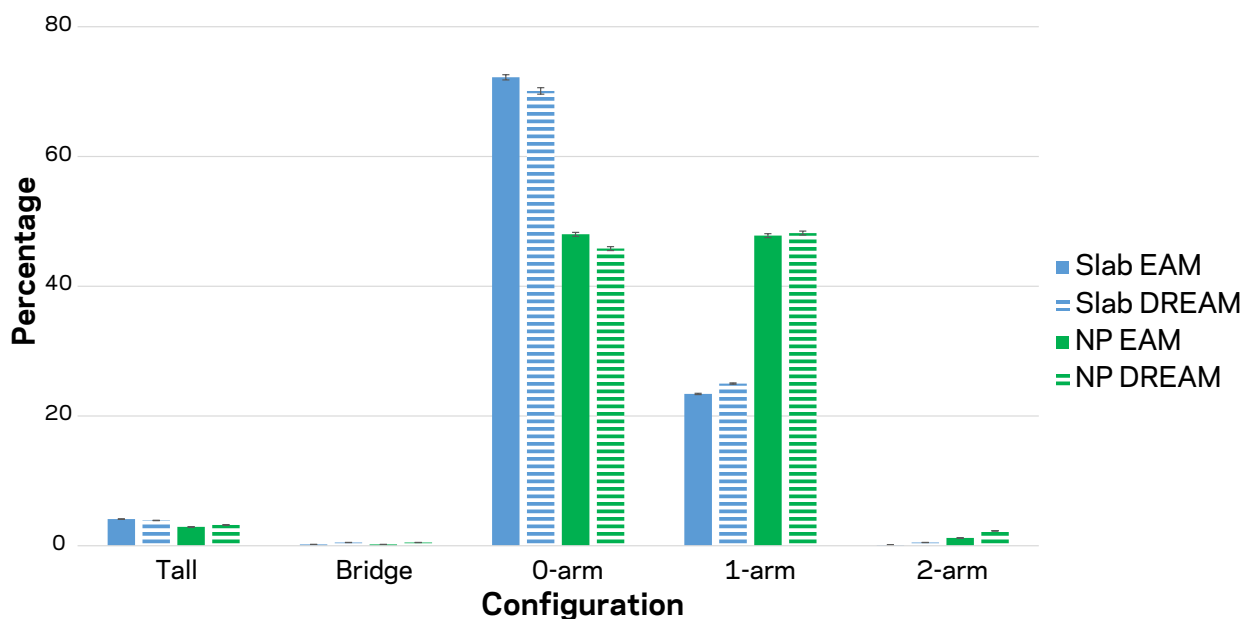


Figure 4: Citrate binding preferences for the non-polarizable Au (111) slab, polarizable Au (111) slab, non-polarizable nanoparticle, and polarizable nanoparticle systems. The error bars are the 95% confidence intervals.

When comparing this data with that of Chong *et al.*, it is clear that nanostructure curvature alters citrate configuration distributions. The systems in this work were constructed with similar concentrations of citrate and sizes of nanostructures as compared to Chong *et al.* All citrate-citrate and citrate-gold interaction parameters are identical. For the Au(111) slabs with both polarizable and non-polarizable force fields, the percentage of citrates bound in the tall and bridge configurations matched those of Chong *et al.* For the Au nanospheres with both polarizable and non-polarizable

force fields, the percentage of citrates bound in the bridge and 1-arm configurations matched those of Chong *et al.* While the increase in curvature does not lead to better agreement with Chong *et al.*, it does demonstrate that this increase leads to a change in configurations. Again, polarization of the gold surface appears to make very little difference in citrate binding preferences when compared with the effect of surface curvature. Differences between the binding statistics reported by Chong *et al.* and those reported here are likely due to different choices of water models and water - metal interactions.

When the citrates were simulated using interaction parameters from Wright *et al.*,³⁰ we did not observe any binding to the gold surface. This is almost certainly due to the larger Lennard-Jones radii of the citrate oxygen atoms in that model. Citrate binding is in direct competition with water binding to the surface, and small changes in $\sigma_{\text{Au-O}}$ can dramatically alter the relative binding energies of the two models.

Thermal Transport Properties

Thermal profiles ($T(z)$) and continuity equation fits for the planar interfaces are shown in Fig. 5. The fits do a reasonably good job of capturing the thermal gradients in the solvent for these systems. Projection of particle and solvent temperatures onto the interface also allows straightforward calculation of the temperature gap between solid and solution phases. The thermal profiles of the planar systems were also compared with identical systems using sodium citrate interaction parameters from Wright *et al.*,³⁰ and with systems solvated in neat water, and all force fields yield nearly identical ΔT values at the planar interface under the same kinetic energy flux. This is reflected in the interfacial thermal conductance values, which are quite similar for the planar interface. All simulations have an average temperature of 300 ± 10 K.

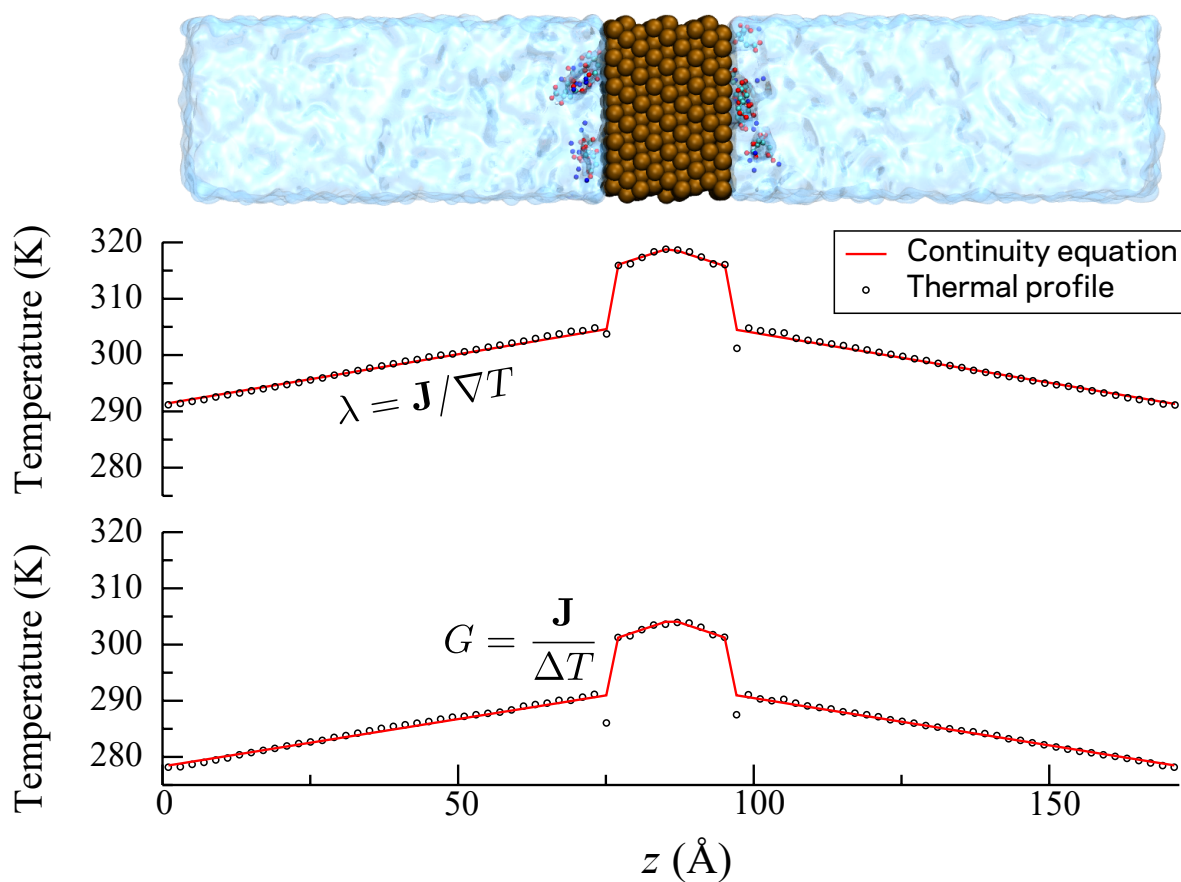


Figure 5: *Top*: An equilibrated planar Au(111) slab, solvated in water and sodium citrate (water is shown here as translucent). *Middle*: Average thermal profile for the non-polarizable (EAM) gold systems (black circles) and a fit of the thermal profile using the continuity equation in Eq. (5) (red line). *Bottom*: The same as the middle panel, but for polarizable gold simulated using the DR-EAM force field. In each case, the thermal profiles are an average of 10 statistically independent simulations.

Calculated thermal transport coefficients for the planar systems are shown in Table 3. Solvent thermal conductivities were calculated for the planar interface systems using Eq. (4). The thermal conductivity values are in good agreement with those for neat SPC/E that were obtained by Armstrong *et al.*³⁶ To compute the interfacial thermal conductance, the continuity fits using Eq. (5) were used to estimate the temperature jumps at the interface. Notably, differences in λ and G for the Chong and Wright citrate models and neat water are relatively small, indicating that the water is dominating the thermal transport in this system.

Table 3: Solvent Thermal Conductivity (λ) and Interfacial Thermal Conductance (G) Values for Systems Containing Au(111) planar interfaces

Solution Phase	Metal	λ ($\text{Wm}^{-1} \text{K}^{-1}$)	G ($\text{MW m}^{-2} \text{K}^{-1}$)
0.12 M Sodium citrate (parameters from Chong <i>et al.</i> ²⁰)	non-polarizable	0.97 ± 0.03	170 ± 4
	polarizable	1.07 ± 0.05	176 ± 10
0.12 M Sodium citrate (parameters from Wright <i>et al.</i> ³⁰)	non-polarizable	1.00 ± 0.03	169 ± 8
	polarizable	1.04 ± 0.04	170 ± 11
Neat Water	non-polarizable	1.03 ± 0.07	171 ± 9
	polarizable	1.07 ± 0.08	198 ± 14

In order to aid in interpreting differences in behavior between the planar and nanoparticle systems, the number densities, $n(z)$ and $n(r)$, for the various species are shown in Figure 6. We observe that water dominates the first solvation layer directly adjacent to the gold nanospheres, while the citrate and sodium ions have their highest concentrations in the second and third solvation layers. In the planar systems, the citrate (and sodium) have some presence immediately above the first solvation layer, and have appreciable concentrations extending up to 30 Å away from the surface.

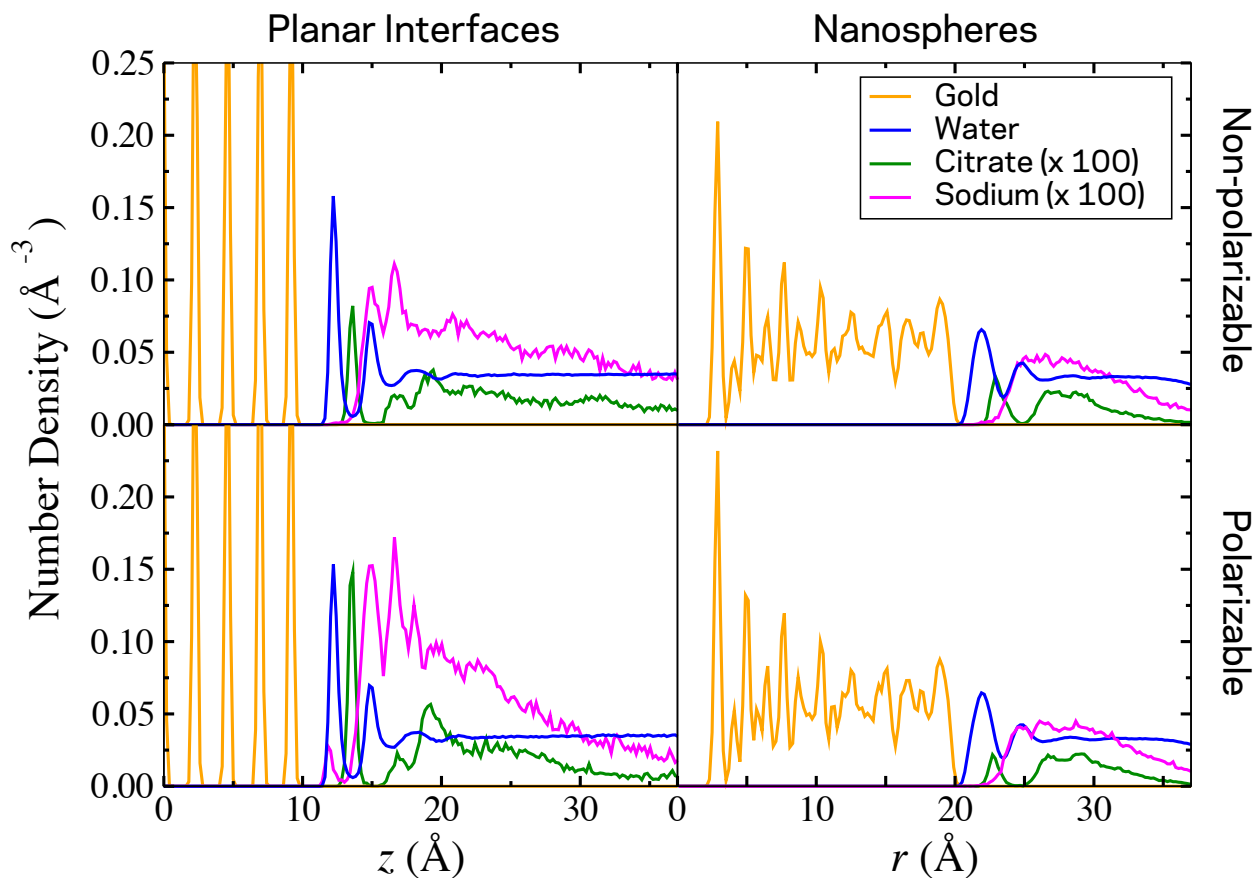


Figure 6: Number density (molecules \AA^{-3}) for each species present in the simulations. *Left:* Planar interfaces, shifted so the center of the metal slab is at $z = 0$. *Right:* Nanospheres, centered at $r = 0$. *Top:* Simulations using a non-polarizable model (EAM) for the metal. *Bottom:* Simulations using the DR-EAM polarizable model for the metal. Note, in all figures, the number densities of the citrate ions and sodium counter-ions have been multiplied by a factor of 100 to aid visibility. Notably, the water and ions surrounding the nanospheres are significantly less structured in the interfacial layers compared with the planar interfaces. Surface polarizability appears to have only a minor influence on the density of any species as a function of distance from the surface. Each curve is an average of 10 statistically independent simulations.

Fig. 7 illustrates typical thermal profiles ($T(r)$) for both the non-polarizable and polarizable nanoparticle systems. Fits from Eq. (8) are also shown, and we note that these provide a relatively poor representation of solvent layering effects.

For the nanoparticle systems, the series approximation for the Kapitza resistance in Eq. (9) was used to compute G . Because the citrate and sodium counter ions form diffuse layers surrounding the particles, defining the overall width of the interface is important to capturing the interfacial conductance. The inner radius for the interface was set to 17.75 Å, a radius which is unambiguously inside the gold particle (see Fig. 6), and G was calculated from that location to an outer boundary that was unambiguously within the solvent cloud. r values of 22.25, 24.25, 26.25, 28.25, and 30.25 Å give effective Kapitza (interfacial) widths of 4.50, 6.50, 8.50, 10.50, and 12.50 Å, respectively. In Fig. 7, we also indicate the inner boundary of the Kapitza series approximation and the range of values for the outer boundary of this region. Tabulated G values using Eq. (9) for the nanosphere systems are given in Table 4. Despite varying the interfacial widths, the calculated value of G remains relatively stable.

Table 4: Interfacial Thermal Conductance (G) Values in $\text{MW m}^{-2} \text{K}^{-1}$ for citrate-solvated 20 Å nanoparticles using a series of Kapitza resistance values (Eq. (9)).

Metal	Solvent	Kapitza Interface Width				
		4.50 Å	6.50 Å	8.50 Å	10.50 Å	12.50 Å
non-polarizable	0.126 M citrate	361 ± 23	368 ± 27	394 ± 26	373 ± 32	329 ± 18
	neat water	389 ± 46	409 ± 50	391 ± 42	386 ± 42	376 ± 44
polarizable	0.126 M citrate	583 ± 105	532 ± 85	584 ± 116	580 ± 150	510 ± 103
	neat water	694 ± 175	718 ± 198	672 ± 159	684 ± 181	618 ± 115

The use of the continuity equation, Eq. (8), for the spherical systems requires projecting a temperature drop at the location of the nanoparticle surface. This results in a significant underestimate of the temperature drop from the particle surface across the diffuse citrate-water layers. The continuity equations therefore yield significantly higher values of G than the ones obtained using Eq. (9). For completeness, the projections onto the fixed particle radius of 20 Å yield G

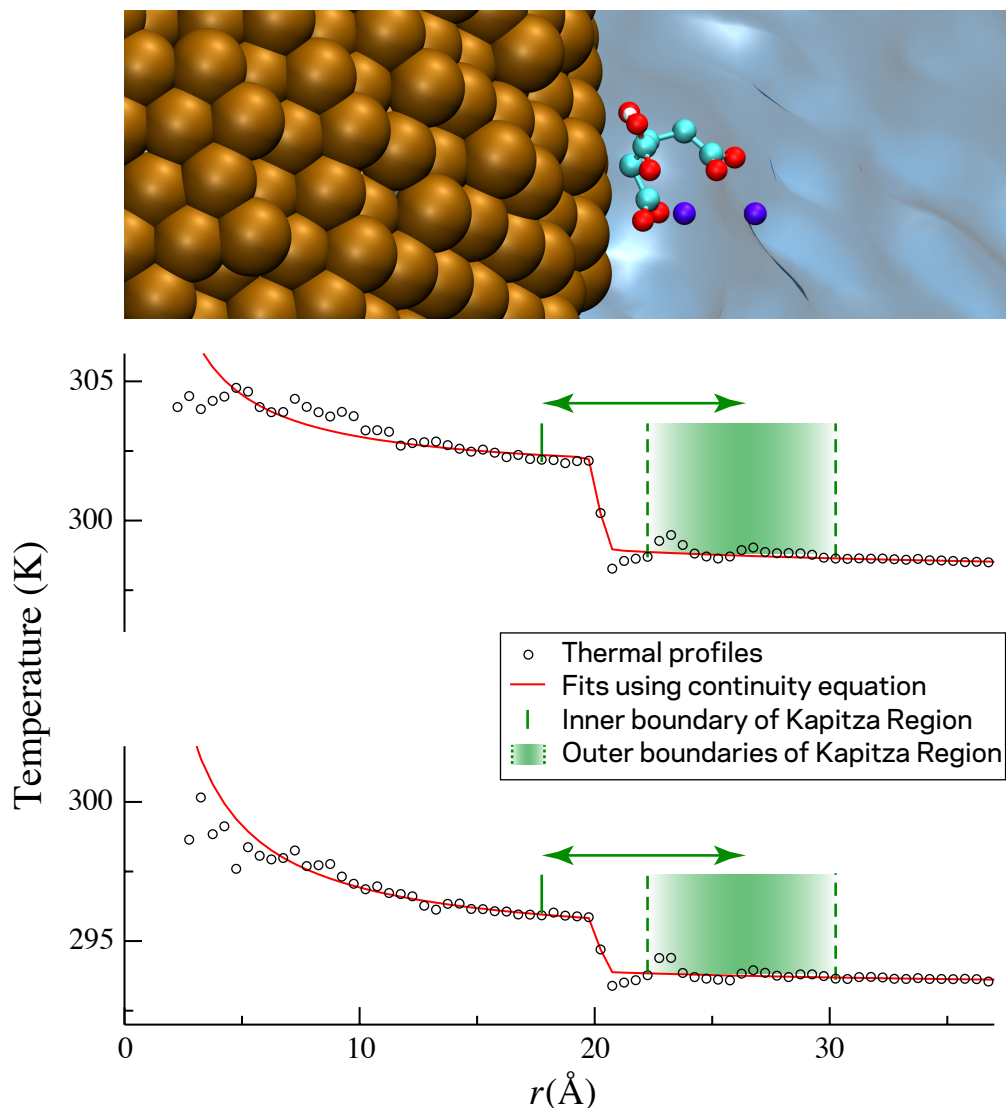


Figure 7: *Top*: A magnified view of one configuration from a nanoparticle simulation showing the presence of a citrate anion. *Middle*: Averaged thermal profile for the nanoparticle systems simulated without polarizability. Continuity equation (Eq. (8)) fits to the thermal profile are shown in red, and the boundaries of the Kapitza regions for Eq. (9) are shown in green. *Bottom*: Averaged thermal profile for the polarizable (DR-EAM) nanoparticle systems. Note that the Kapitza series approximation provides a more stable and repeatable estimate of interfacial thermal conductance than continuity fits.

values of 915 ± 48 and 1004 ± 160 $\text{MW m}^{-2} \text{K}^{-1}$ for non-polarizable gold with citrate and neat water, respectively. With the use of polarizability, these values jump to 1661 ± 403 and 1650 ± 329 $\text{MW m}^{-2} \text{K}^{-1}$, respectively. These do not appear to be reliable estimates of the true interfacial thermal conductance when the interface has spatial extent due to surface binding of an adsorbed

species.

For both planar and nanoparticle interfaces, polarizing the gold surface leads to an increase in G . Our explanation for this is the same as that of Bhattarai *et al.* The image charge and image dipole interactions present in the DR-EAM potential enhance the binding strength of *all* polar species, leading to enhanced coupling between the motion of solid and liquid phases, thereby enhancing thermal transport.²³ For the planar interfaces, polarization of the gold surface does not appear to impact either solution-phase conductivity or interfacial thermal conductance. However, polarization of the spherical nanoparticles causes a significant increase in G (see table 4).

In all cases, the calculated interfacial thermal conductance for the nanospheres represents a very large jump ($2.5 \times -4.1 \times$) relative to the planar 111 interface. The nanospheres have a large population of undercoordinated surface metal sites when compared with the planar 111 surface,¹⁰ and this may explain part of the increase in G . However, there is an additional large increase in conductance when polarizability is introduced, so the role that this plays is still an interesting question. In the next section we explore the role that metal polarizability plays on enhancing the low frequency heat-carrying vibrational modes that are experienced by surface molecules on either side of the interface.

Vibrational Power Spectra

Under acoustic impedance mismatch models for interfacial thermal transport, the same phonon frequencies must be present on both sides of the interface in order to scatter a phonon across that boundary. Additionally, lower frequency phonons are most efficient for heat conduction. To explore the role of polarizability we have computed the power spectra for vibrational motion projected in a direction normal to the interface,

$$\rho_{\perp}(\omega) = \frac{1}{\sqrt{2\pi}} \int_{-\infty}^{\infty} \langle v_{\perp}(t) \cdot v_{\perp}(0) \rangle e^{-i\omega t} dt \quad (10)$$

where the angle bracket averages over all particles j , and the perpendicular velocities for those particles,

$$v_{j,\perp}(t) = \mathbf{v}_j(t) \cdot \hat{\mathbf{n}}(\mathbf{r}_j) \quad (11)$$

and $\hat{\mathbf{n}}(\mathbf{r}_j)$ is the unit vector normal to the interface at the location (\mathbf{r}_j) of atom j . In planar systems, the normal direction is the z axis, but for nanoparticles, the radial vector from the particle center determines the normal direction.

We divided the systems into three regions, interfacial gold (within 5 Å of the interface), interfacial solvent (also within 5 Å of the interface), and non-interfacial solvent (more than 10 Å away from the interface) for both the planar and nanoparticle systems. Each system was simulated for an additional 50 ps in the NVE ensemble for the planar systems and the Langevin Hull (NPT) for the nanoparticle systems. Velocity autocorrelation functions with a time granularity of 3 fs were calculated from these trajectories. The power spectra are discrete Fourier transforms of these autocorrelation functions.

Vibrational power spectra for the planar systems are shown in Figure 8. There is a reduction in the lowest frequency modes in the interfacial solvent relative to the non-interfacial region, regardless of gold polarizability. Application of the DR-EAM potential (middle panel) more heavily populates the 300 cm^{-1} region of the spectrum when compared with the EAM systems, but the effect is quite small. As one might expect, metal polarizability makes some changes to the gold spectrum, but in the planar systems, this consists of a shift of modes from $\sim 100 \text{ cm}^{-1}$ to $\sim 120 \text{ cm}^{-1}$. At lower frequencies, there appears to be very little motion of the vibrational modes due to polarizability

The vibrational power spectra for the nanoparticle systems are shown in Figure 9. The same decrease in low frequency heat carrying modes in the interfacial solvent is present. The bottom panels of Figures 8 and 9 show the running average of the difference between spectra for the DR-EAM systems and the EAM systems where $\Delta\rho(\omega) = \rho(\omega)_{\text{DR-EAM}} - \rho(\omega)_{\text{EAM}}$. The most notable differences when compared with the planar systems in Fig. 8, is the larger effect on the metal modes near 80 and 120 cm^{-1} . The surface metal atoms exhibit a migration from lower

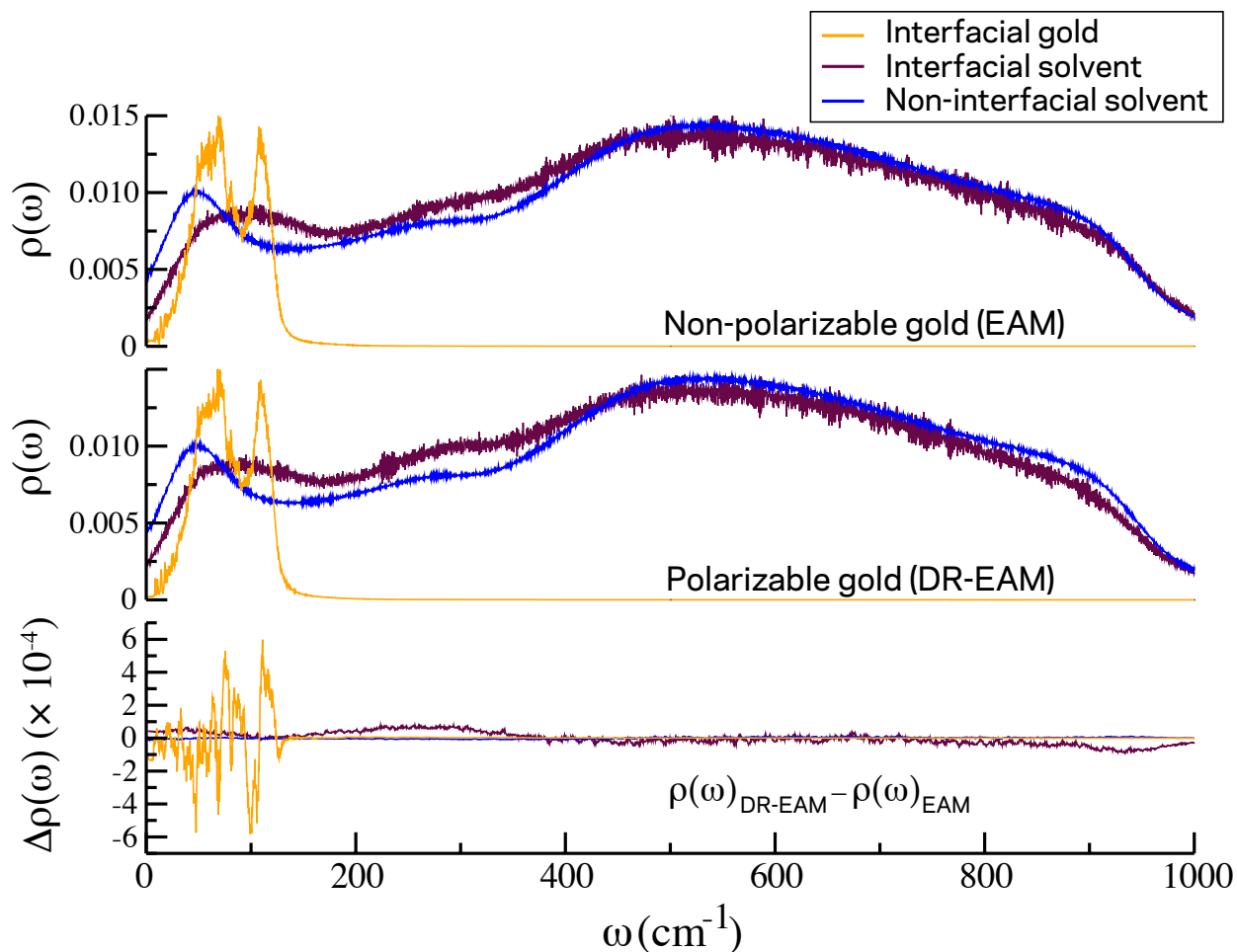


Figure 8: Normalized vibrational power spectra, which have been projected in a direction normal to the interface, for the planar gold systems. Spectra are shown for interfacial gold (within 5 Å of the interface), interfacial solvent (also within 5 Å of the interface), and non-interfacial solvent (more than 10 Å away from the interface). Each curve is an average of 10 statistically independent simulations. *Top*: simulations using a non-polarizable model for gold (EAM). *Middle*: simulations using polarizable gold (DR-EAM). *Bottom*: differences in these spectra, showing that although the metal surface atoms exhibit some spectral changes, metal polarizability has only a small effect on solvent vibrations. (Note that the solvent curves in the upper two panels are magnified by a factor of 10 to aid visibility.)

frequency ($< 60 \text{ cm}^{-1}$) modes to these two new bands. Additionally, when polarizability is added to the nanoparticles, there are changes in the vibrational modes exhibited by the solvent, with a decrease in the low frequency $\omega < 450 \text{ cm}^{-1}$ modes, and an increase in the population of the $500 - 1000 \text{ cm}^{-1}$ range.

At this point, it is unclear how large of an effect the changes in collective vibrational spectra will

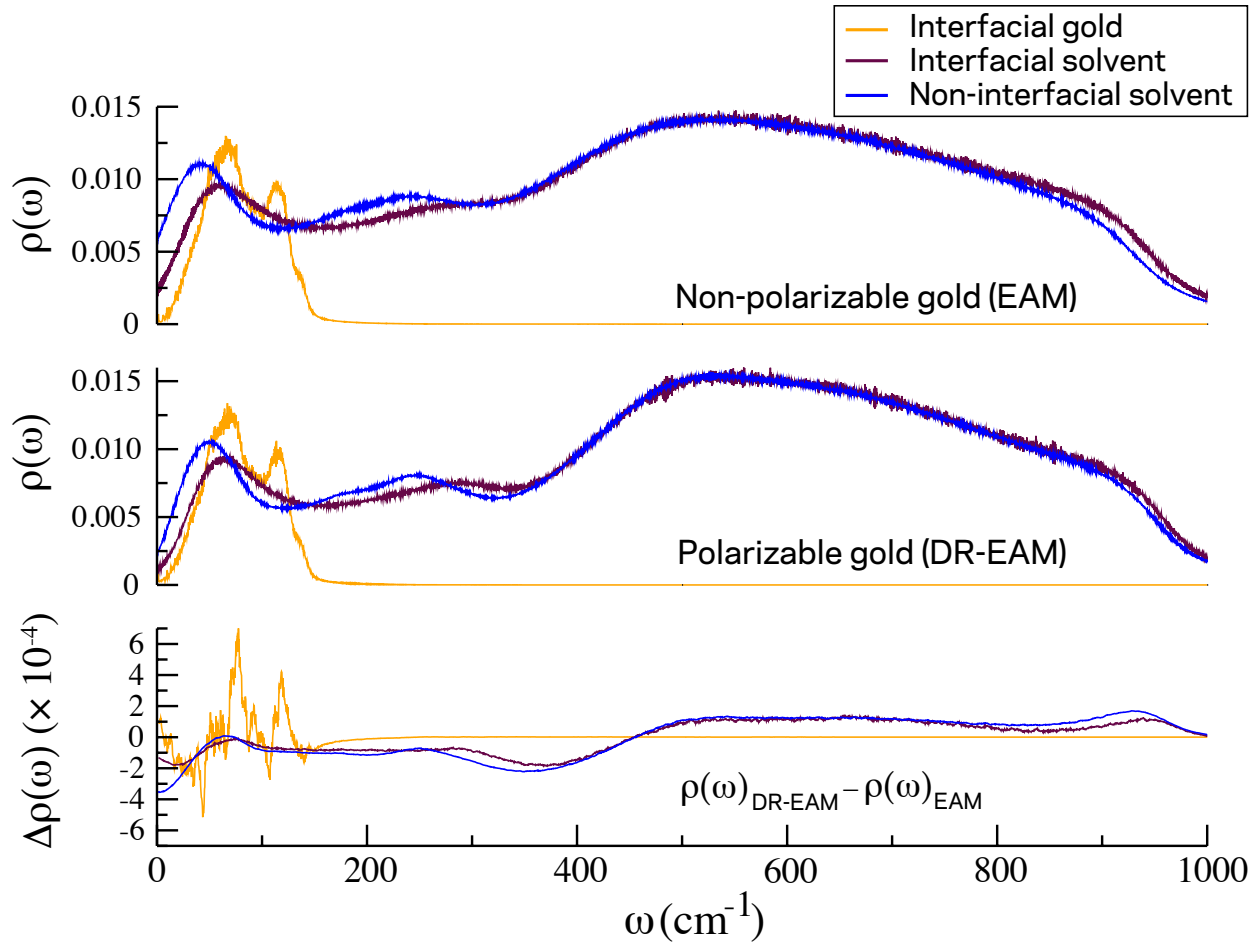


Figure 9: Similar spectra to Fig. 8, but for systems containing nanospheres. The most notable differences when compared with the planar systems in Fig. 8, is the larger effect on the metal modes near 80 and 120 cm^{-1} , and the significant shift of vibrational population from lower to higher frequencies in the solvent.

have on conductance. The magnitudes of the changes due to polarizability are relatively small, and there is a depletion of lower frequency modes which should reduce conductance in most models. A more direct mechanism seems to be that polarizability simply increases the interaction strength between the solvent layer and the metal atoms, effectively enhancing the phonon scattering across the interface, independent of mode frequency.

Charge Penetration in the Metal Interface

The main effect of the polarizable metal force field is that it allows transient partial charges to develop on the metal atoms, enhancing interactions with polar species at the interface. Two interesting questions are the degree of polarization, i.e., the magnitude of the excess partial charges, and also the depth of penetration of this polarization into the metal. To answer these questions, we calculated the excess charge density (as a function of z for the planar interfaces and r for the nanospheres). Note that the metal structure has been recentered at $z = 0$ or $r = 0$ to make a visible comparison between these systems. This data is shown in Fig. 10. When DR-EAM is utilized, the charges on the gold atoms in the layers closest to the surface respond to nearby solvent molecules. This charge penetration extends only to the first two atomic layers of the gold. On average, the first (skin) layer of metal maintains a small negative charge density, which is largely a response to the solvent environment in closest proximity to the interface. That is, when one of the water hydrogens points at the surface, the local response is a net negative polarization of the adjacent surface gold atoms. The metallic layer below this largely reacts with a net positive charge density, conserving total charge in the metal, and effectively neutralizing local fields at sites internal to the metal structure. In the original work parameterizing DR-EAM, this behavior was also observed in layered metallic structures responding to a uniform electric field.²³

The gold atoms in the spherical nanoparticles respond to nearby atoms with a significantly larger magnitude of charge density. The surface atoms in the nanospheres have fewer metallic neighbors which can spread out the polarization response, and are in contact with a larger solid angle of the solvent. The polarization response directly increases the interaction strength with nearby polar solvent molecules, so the larger interfacial conductance in these systems is not surprising.

In the solvent, there is a significant oscillation of the charge density in the first 7-10 Å adjacent to the metal surface. This is largely due to orientational preferences in the water at the surface. This has been observed for planar gold surfaces, with orientational correlations also extending 7-10 Å from the surface.²⁴ Similar water orientational preferences have also been observed for water confined between graphene sheets.³⁷

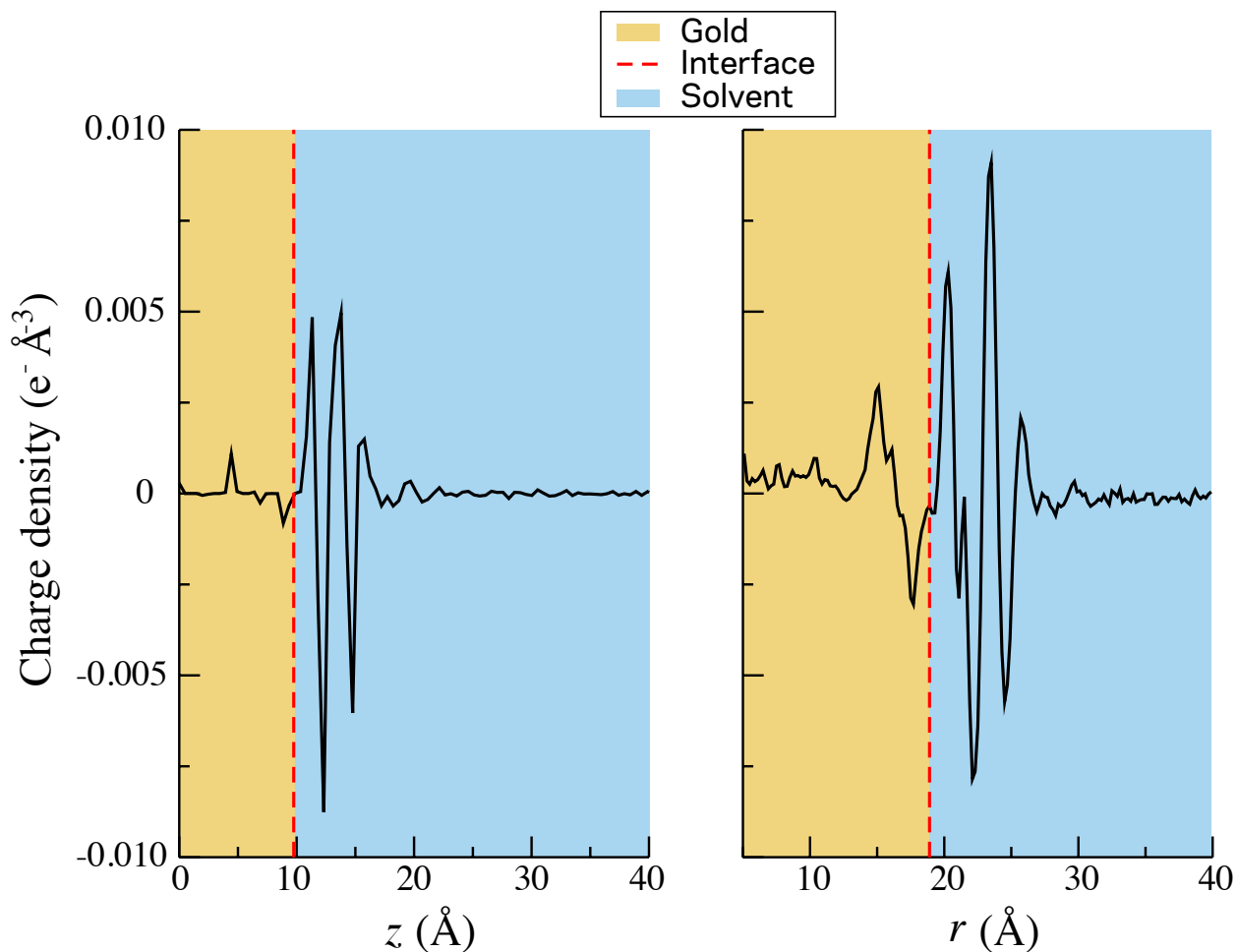


Figure 10: *Left*: Excess charge density as a function of z for DR-EAM planar interfaces (with the metal slab centered at $z = 0$). The red dashed line denotes the approximate location of the metal-solvent interface. *Right*: Charge density as a function of r for DR-EAM nanoparticle systems. Note that the polarizability of the metal produces significantly larger surface charge density in the nanospheres than in the planar interfaces. The oscillatory charge density in the solution phase is largely due to water orientational preferences at the metal surface that damp out after a few solvent layers.

The charge density plot partly helps to answer why we see polarization-induced enhancement in thermal conductance. Adsorbed water layers have orientational preferences at interfaces, and with a polarizable metal surface, these preferences point partial charges from the water directly at the surface, creating opposing image charges at the interface. The image charge effect increases the effective interaction strength between the water and the metal. What Fig. 10 also shows is that in the nanospheres, this effect is approximately a factor of four larger than in the planar interface,

which goes a long way to explaining the $2.5 - 4.1 \times$ jump in G values between the two systems.

Conclusions

We have used molecular dynamics simulations of citrate-capped gold nanostructures to make four separate determinations: The binding preferences of citrate molecules on different gold surfaces, the thermal transport properties near the interface, the vibrational power spectra on both sides of the interface, and charge penetration and degree of polarization at the interface. The main conclusion from the binding studies was that citrate binding is more heavily influenced by nanostructure curvature rather than surface polarization. Polarization does, however, lead to an increase in the interfacial thermal conductance in all systems studied. This increase in G is much more pronounced in the nanoparticle systems. Polarization also causes a small increase in solvent thermal conductivity, λ , near the metal surface in the planar systems.

We also studied an alternative citrate model that does not require internal constraints,³⁰ but we were subsequently unable to induce citrate binding, under competition with the water binding to the surface. It is possible that a minor refitting of the Au-X interaction lengths would result in an all atom citrate model that could bind under aqueous conditions.

Another finding is that for interfaces which are “fuzzy” or which have a broad extent away from the solid-liquid boundary, projecting temperature jumps onto an artificial interface using continuity equations can be problematic, as ΔT is often an underestimate of the temperature drop across the boundary layers. For the planar systems, the thermal profiles were well-defined and had little alterations due to solvent layering effects, and a projection approach was suitable. In the nanospheres, however, we determined that our modified continuity equations for calculating G must be used with caution. Alternatively, we have shown that the value of G remains fairly stable with varying lengths of the region used for calculating the Kapitza resistance from a series of concentric shells.

Comparisons of vibrational power spectra for the polarizable vs. non-polarizable models are

interesting, but inconclusive. In some frequency ranges, we see a polarizability enhancement for the nanoparticles, but these do not appear to be large enough to predict a change in conductance. However, the charge density (Fig. 10) points to the most likely explanation for the large G values for the polarizable nanospheres, as surface atoms are significantly more polarized in the spherical structures than in the planar structures, leading to a large increase in the effective metal-to-solvent interaction strength.

One interesting question is whether other biologically-compatible surface capping agents, e.g. polyethylene glycol and cetrimonium bromide (CTAB), yield similar changes to thermal transport properties given that their binding mechanism and methods of preventing aggregation are somewhat different from the action of sodium citrate. In all three cases, however, the proximity of dipolar solvent or charged ionic species will require careful treatment of metal surface polarizability.

Acknowledgement

Support for this project was provided by the National Science Foundation under grants CHE-1663773 and CHE-1954648. Computational time was provided by the Center for Research Computing (CRC) at the University of Notre Dame. The authors would also like to express their thanks to Gene Chong and Rigoberto Hernandez for helpful conversations on implementing the citrate force field.

Supporting Information Available

Details of system composition, force field parameters, equilibration, and data collection, further citrate configuration analysis, and additional vibrational power spectra for the systems described in this work.

References

- (1) Alkilany, A. M.; Murphy, C. J. Toxicity and cellular uptake of gold nanoparticles: what have we learned so far? *J. Nanopart. Res.* **2010**, *12*, 2313–2333.
- (2) Elahi, N.; Kamali, M.; Baghersad, M. H. Recent biomedical applications of gold nanoparticles: a review. *Talanta* **2018**, *184*, 537–556.
- (3) Li, N.; Zhao, P.; Astruc, D. Anisotropic Gold Nanoparticles: Synthesis, Properties, Applications, and Toxicity. *Angew. Chem. Int. Ed.* **2014**, *53*, 1756–1789.
- (4) Duta, S.; Bellucci, L.; Agostini, M.; Gagliardi, M.; Corni, S.; Cecchini, M.; Brancolini, G. Atomistic simulations of gold surface functionalization for nanoscale biosensors applications. *Nanotechnology* **2021**, *32*, 095702.
- (5) Monti, S.; Jose, J.; Sahajan, A.; Kalarikkal, N.; Thomas, S. Structure and dynamics of gold nanoparticles decorated with chitosan-gentamicin conjugates: ReaxFF molecular dynamics simulations to disclose drug delivery. *Phys. Chem. Chem. Phys.* **2019**, *21*, 13099–13108.
- (6) Gopalakrishnan, R.; Singam, E. A.; Sundar, J. V.; Subramanian, V. Interaction of collagen like peptides with gold nanosurfaces: a molecular dynamics investigation. *Phys. Chem. Chem. Phys.* **2015**, *17*, 5172–5186.
- (7) Sztandera, K.; Gorzkiewicz, M.; Klajnert-Maculewicz, B. Gold nanoparticles in cancer treatment. *Mol. Pharmaceutics* **2019**, *16*, 1–23.
- (8) Liu, X.; Jiuan Chen, H.; Chen, X.; Parini, C.; Wen, D. Low frequency heating of gold nanoparticle dispersions for non-invasive thermal therapies. *Nanoscale* **2012**, *4*, 3945–3953.
- (9) Essajai, R.; Mzerd, A.; Hassanain, N.; Qjani, M. Thermal conductivity enhancement of nanofluids composed of rod-shaped gold nanoparticles: Insights from molecular dynamics. *J. Mol. Liq.* **2019**, *293*, 111494.

- (10) Neidhart, S. M.; Gezelter, J. D. Thermal Transport is Influenced by Nanoparticle Morphology: A Molecular Dynamics Study. *J. Phys. Chem. C* **2018**, *122*, 1430–1436.
- (11) Jiang, M.; Olarte-Plata, J. D.; Bresme, F. Atomistic Nodal Approach: a General Molecular Dynamics Method for Computing Local Thermal Conductance at Atomistic Resolution. *J. Chem. Phys.* **2022**, *156*, 044701.
- (12) Cheraghipour, E.; Tamaddon, A.; Javadpour, S.; Bruce, I. PEG conjugated citrate-capped magnetite nanoparticles for biomedical applications. *J. Magn.* **2013**, *328*, 91–95.
- (13) Raji, V.; Kumar, J.; Rejiya, C.; Shenoi, M. V. V. N.; Abraham, A. Selective photothermal efficiency of citrate capped gold nanoparticles for destruction of cancer cells. *Exp. Cell Res.* **2011**, *317*, 2052–2058.
- (14) Vechia, I. C. D.; Steiner, B. T.; Freitas, M. L.; dos Santos Pedroso Fidelis, G.; Galvani, N. C.; Ronchi, J. M.; Possato, J. C.; Ívens Fagundes, M.; Rigo, F. K.; Feuser, P. E. et al. Comparative cytotoxic effect of citrate-capped gold nanoparticles with different sizes on noncancerous and cancerous cell lines. *J. Nanopart. Res.* **2020**, *22*, 133.
- (15) Kamiński, M.; Jurkiewicz, K.; Burian, A.; Bródka, A. The structure of gold nanoparticles: molecular dynamics modeling and its verification by X-ray diffraction. *J. Appl. Cryst.* **2020**, *53*, 18.
- (16) Meena, S. K.; Sulpizi, M. Understanding the Microscopic Origin of Gold Nanoparticle Anisotropic Growth from Molecular Dynamics Simulations. *Langmuir* **2013**, *29*, 14954–14961.
- (17) Lai, C.-T.; Sun, W.; Palekar, R. U.; Thaxton, C. S.; Schatz, G. C. Molecular Dynamics Simulation and Experimental Studies of Gold Nanoparticle Templated HDL-Like Nanoparticles for Cholesterol Metabolism Therapeutics. *ACS Appl. Mater. Interfaces* **2017**, *9*, 1247–1254.

- (18) Tavanti, F.; Pedone, A.; Menziani, M. C. Competitive binding of Proteins to Gold Nanoparticles Disclosed by Molecular Dynamics Simulations. *J. Phys. Chem. C* **2015**, *119*, 22172–22180.
- (19) Wright, L.; Rodger, M.; Walsh, T. Structure and Properties of Citrate Overlayers Adsorbed at the Aqueous Au(111) Interface. *Langmuir* **2014**, *30*, 15171–15180.
- (20) Chong, G.; Laudadio, E.; Wu, M.; Murphy, C.; Hamers, R.; Hernandez, R. Density, Structure, and Stability of Citrate³⁻ and H₂citrate⁻ on Bare and Coated Gold Nanoparticles. *J. Phys. Chem. C* **2018**, *122*, 28393–28404.
- (21) Chong, G.; Hernandez, R. Adsorption Dynamics and Structure of Polycations on Citrate-Coated Gold Nanoparticles. *J. Phys. Chem. C* **2018**, *122*, 19962–19969.
- (22) Perfilieva, O.; Pyshnyi, D.; Lomzov, A. Molecular Dynamics Simulation of Polarizable Gold Nanoparticles Interacting with Sodium Citrate. *J. Chem. Theory Comput.* **2019**, *15*, 1278–1292.
- (23) Bhattarai, H.; Newman, K.; Gezelter, J. Polarizable potentials for metals: The density re-adjusting embedded atom method (DR-EAM). *Phys. Rev. B* **2019**, *99*, 094106.
- (24) Bhattarai, H.; Newman, K.; Gezelter, J. The role of polarizability in the interfacial thermal conductance at the gold-water interface. *J. Chem. Phys.* **2020**, *153*, 204703.
- (25) Kuang, S.; Gezelter, J. Velocity shearing and scaling RNEMD: a minimally perturbing method for simulating temperature and momentum gradients. *Mol. Phys.* **2012**, *110:9-10*, 691–701.
- (26) Stocker, K.; Gezelter, J. A Method for Creating Thermal and Angular Momentum Fluxes in Nonperiodic Simulations. *J. Chem. Theory Comput.* **2014**, *10*, 1878–1886.
- (27) Neidhart, S.; Gezelter, J. Thermal Conductivity of Gold-Phenylethanethiol (Au₁₄₄PET₆₀) Nanoarrays: A Molecular Dynamics Study. *J. Phys. Chem.* **2020**, *124*, 3389–3395.

- (28) Lervik, A.; Bresme, F.; Kjelstrup, S. Heat transfer in soft nanoscale interfaces: the influence of interface curvature. *Soft Matter* **2009**, *5*, 2407–2414.
- (29) Hu, M.; Poulikakos, D.; Grigoropoulos, C.; Pan, H. Recrystallization of picosecond laser-melted ZnO nanoparticles in a liquid: A molecular dynamics study. *Soft Matter* **2010**, *132*, 164504.
- (30) Wright, L.; Rodger, M.; Walsh, T. Aqueous citrate: a first-principles and force-field molecular dynamics study. *RSC Adv.* **2013**, *3*, 16399–16409.
- (31) Berendsen, H.; Grigera, J.; Straatsma, T. The Missing Term in Effective Pair Potentials. *J. Phys. Chem.* **1987**, *91*, 6269–6271.
- (32) Dou, Y.; Zhigilei, L. V.; Winograd, N.; Garrison, B. J. Explosive Boiling of Water Films Adjacent to Heated Surfaces: A Microscopic Description. *J. Phys. Chem. A* **2001**, *105*, 2748–2755.
- (33) Zhou, X.; Johnson, R.; Wadley, H. Misfit-energy-increasing dislocations in vapor-deposited CoFe/NiFe multilayers. *Phys. Rev. B* **2004**, *69*, 144113.
- (34) Gezelter, J.; Bhattarai, H.; Drisko, C.; Duraes, A.; Lin, T.; Vardeman, C.; Fennell, C.; Meineke, M.; Loudon, P.; Neidhart, S. et al. *OpenMD, an Open Source Engine for Molecular Dynamics*, Version 2.6; <http://openmd.org>. Accessed January 11, 2022.
- (35) Martínez, L.; Andrade, R.; Birgin, E.; Martínez, J. Packmol: A package for building initial configurations for molecular dynamics simulations. *J. Chem. Comput.* **2009**, *30(13)*, 2157–2164.
- (36) Armstrong, J.; Lervik, A.; Bresme, F. Enhancement of the Thermal Polarization of Water via Heat Flux and Dipole Moment Dynamic Correlations. *J. Phys. Chem. B.* **2013**, *117*, 14817–14826.

- (37) Cicero, G.; Grossman, J. C.; Schwegler, E.; Gygi, F.; Galli, G. Water Confined in Nanotubes and between Graphene Sheets: A First Principle Study. *Journal of the American Chemical Society* **2008**, *130*, 1871–1878.

TOC Graphic

